Journal of Inorganic Biochemistry 264 (2025) 112810

Contents lists available at ScienceDirect

Journal of Inorganic Biochemistry

journal homepage: www.elsevier.com/locate/jinorgbio

Structural insights into temperature-dependent dynamics of METPsc1, a miniaturized electron-transfer protein

Luigi F. Di Costanzo [a,*], Gianmattia Sgueglia [b], Carla Orlando [c], Maurizio Polentarutti [d], Linda Leone [b], Salvatore La Gatta [b], Maria De Fenza [b], Luca De Gioia [c], Angela Lombardi [b], Federica Arrigoni [c], Marco Chino [b,*]

[a] Department of Agricultural Sciences, University of Naples Federico II, Via Università 100, 80055 Portici, NA, Italy
[b] Department of Chemical Sciences, University of Naples Federico II, Via Cintia 21, 80126 Napoli, Italy
[c] Department of Biotechnology and Biosciences, University of Milan-Bicocca, Piazza della Scienza 2, 20126 Milan, Italy
[d] Elettra-Sincrotrone Trieste, S.S. 114 km 163.5, Basovizza 34149, Trieste, Italy

ARTICLE INFO

Keywords:
Artificial metalloprotein
Temperature-dependent crystallography
Protein dynamics
Cadmium coordination
Protein design
Electron transfer

ABSTRACT

The design of protein-metal complexes is rapidly advancing, with applications spanning catalysis, sensing, and bioremediation. We report a comprehensive investigation of METPsc1, a Miniaturized Electron Transfer Protein, in complex with cadmium. This study elucidates the impact of metal coordination on protein folding and structural dynamics across temperatures from 100 K to 300 K. Our findings reveal that METPsc1, composed of two similar halves stabilized by intramolecular hydrogen bonds, exhibits a unique “clothespin-like” recoil mechanism. This allows it to adapt to metal ions of varying radii, mirroring the flexibility observed in natural rubredoxins. High-resolution crystallography and molecular dynamics simulations unveil concerted backbone motions and subtle temperature-dependent shifts in side-chain conformations, particularly for residues involved in crystal packing. Notably, Cd—S bond lengths increase with temperature, correlating with anisotropic motions of the sulfur atoms involved in second-shell hydrogen bonding. This suggests a dynamic role of protein matrix upon redox cycling. These insights into METPsc1 highlight its potential for catalysis and contribute to the designing of artificial metalloproteins with functional plasticity.

1. Introduction

Protein design has rapidly evolved into a cutting-edge approach in biotechnology and molecular biology, driven by the continuous advancements in rational approaches and computational chemistry [1–5]. This progress facilitates the precise prediction of 3D protein architectures and allows the crafting of proteins with novel shapes and molecular functions even from scratch [6–12]. Among the myriad possibilities in protein design, the creation of protein-metal complexes stands out as a particularly promising avenue. Leveraging their catalytic capabilities, these complexes have emerged as powerful tools with diverse applications in catalysis, sensing, electron transfer protein, and the modeling of novel metalloenzymes [13–19]. Designing such complexes often entails customizing amino acid sequences to create specific binding sites for metal ions and to modulate their catalytic cycles.

A bottleneck in designing these metal complexes lies in the dynamic nature of proteins and the need to select residues with proper metal coordination geometry undergoing specific catalytic cycles under various conditions. Protein dynamics encompass conformational changes, folding/unfolding processes, and the dynamics of active sites, all of which play a critical role in their biological functions [20,21]. These dynamics are driven by thermal motion, covering time scales that range from individual bond vibrations (femtosecond scale) to fluctuations in chemical groups (nanoseconds to microseconds) and even longer times, encompassing larger segments of molecules [22–24]. Notably, research on key enzymes at room temperature revealed subtle structural shifts compared to cryogenic temperatures [23,24].

A recent milestone in protein design of metal-protein complexes is represented by a miniature 28-residue protein named METPsc1 (Miniaturized Electron Transfer Protein single chain), which serves as the minimal unit needed to reproduce rubredoxin (Rd) folding (Fig. 1) [25]. This protein integrates the fundamental elements required for precise

---

* Corresponding authors.
E-mail addresses: luigi.dicostanzo4@unina.it (L.F. Di Costanzo), marco.chino@unina.it (M. Chino).

https://doi.org/10.1016/j.jinorgbio.2024.112810
Received 2 October 2024; Received in revised form 30 November 2024; Accepted 7 December 2024

geometry around a $FeCys_4$ redox center, facilitating efficient electron transfer.

This achievement addressed a significant challenge in de novo protein design as revealed by the close matches of intended design at the sub-Å scale with the crystal structure, at cryogenic temperature, of the designed tetra-thiolate metal-binding protein METPsc1 in complex with zinc ion. This structural agreement establishes a robust connection between its 3D structure and spectroscopic/electrochemical properties. Furthermore, this miniature protein exhibits a high reduction potential when compared to both natural and designed $FeCys_4$-containing proteins and can function as an electron acceptor in a fully artificial chain, initiated by visible light [26–28].

To further explore the influence of metal coordination on protein dynamics and function, we have investigated the METPsc1 protein in complex with cadmium(II), a soft metal ion known for its strong affinity for tetrathiolate motifs, which aligns with the predictions of the *hard-soft acid-base* (HSAB) theory. This choice was motivated by the desire to probe the effects of metal ion substitution on protein folding of a miniaturized protein and structural dynamics across a range of temperatures, from cryogenic to room temperature. While traditional protein crystallography often relies on cryogenic temperatures, our approach allows us to assess the designed protein's behavior under more physiologically relevant conditions and compare its dynamics to those observed in natural proteins.

In this study, we specifically focus on the correlation between local protein B-factors and temperature-induced conformational changes within our designed protein. By analyzing these aspects across a range of temperatures, we aim to reveal dynamic correlations with rigid body motion and/or distinct scattering and crystal properties, with a focus on understanding how the metal center contributes to these behaviors.

2. Materials and methods

2.1. Materials

All the reagents have been purchased from Merck (Darmstadt, Germany). Solvents have been purchased from Romil (Waterbeach, England).

2.2. Solid-phase peptide synthesis

An ABI 433A peptide synthesizer (Applied Biosystem, Foster City, CA, USA) was used. METPsc1 was synthesized with standard Fmoc chemistry on a 0.25 mmol scale, as previously described [25].

2.3. Crystallography

The CdMETPsc1 complex was crystallized by the hanging drop vapor diffusion method at 20 °C. Typically, a drop containing 2.0 μL of 1:1 (*v*/v) mixture of protein solution (10 mg/mL, 7 mM dithiothreitol, 4 mM $CdCl_2$) and 2.0 μL of precipitant buffer (0.1 M HEPES at pH 7.5, 1.4 M sodium citrate tribasic dihydrate) was equilibrated against 0.5 mL reservoir of precipitant buffer. Crystals of the CdMETPsc1 complex grew as long needles with typical dimension of 0.2 × 0.2 × 0.6 mm^3. Upon transferring to the same mother liquor solution, augmented with 30 % 2-methyl-2,4-pentanediol (MPD) solution and flash cooled, crystals yielded diffraction data to 1.28 Å resolution at the XRD1 beamline (Elettra Synchrotron Light Source, Trieste, Italy), using a wavelength of 1.000 Å, and kept at 100 K. Data were processed using XDS [29] and POINTLESS (version 1.11.21) [30]. Crystals presented an orthorhombic unit cell with space group $C222_1$. No twinning was detected.

Diffraction data collections at different temperatures (100 K, 130 K, 160 K, 200 K, and 300 K) were performed from the same large crystal with a gradual raising of the temperature. To improve stability and prevent dehydration during repeated data collection, the cryoprotected crystal was also immersed in paratone oil. The same crystal was used for all temperatures, collecting 360 images (0.5° oscillation, 180° total rotation) per dataset. No phase transition was observed, and the unit cell (Table S2) and space group ($C222_1$) remained consistent with the 100 K structure. Due to radiation damage, only 240 images (120°) were used in the analysis, ensuring high completeness (Table S2). Collecting data by cooling from room temperature was not possible due to rapid crystal deterioration.

The CdMETPsc1 structure (100 K data) was determined using single-wavelength anomalous dispersion (SAD) of the cadmium ion (Phenix suite v1.16). Starting phases allowed tracing of tyrosine residues. During the final refinement stage, a total of 26 water molecules were successfully located. The refined model of the CdMETPsc1 complex at 100 K served as the initial model for solving the structure at other temperatures using the difference Fourier technique [31]. Density modification and phase extension (PHENIX "phase and build") facilitated model completion [32]. Subsequently, PHENIX.refine was utilized to anisotropically refine the model, the COOT graphics program for manual inspection/adjustments [33]. 5 % of reflections were reserved for Rfree calculation. Refinement statistics are reported in Table S2.

2.4. Geometry analysis

Cd tetrahedral sites of small molecule complexes were retrieved from

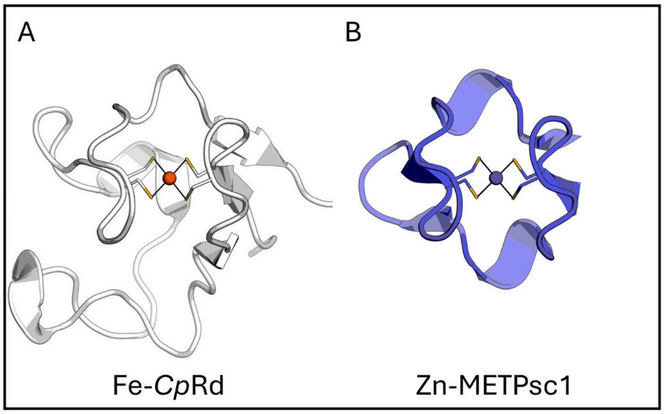

Fig. 1. Comparison between natural protein and miniaturized protein. Crystal structure of *Clostridium pasteurianum* (*Cp*) Rd in complex with iron(III) (A; PDB ID: 1iro). Atomic resolution model of METPsc1 in complex with Zn^{2+} (B; PDB ID: 5sbg). Type I′ β-turn and coordinative cysteine (Cys) residues are highlighted in yellow (B). (For interpretation of the references to colour in this figure legend, the reader is referred to the web version of this article.)

the Cambridge Structural Database (CSD) [34], among those sites that were previously classified by MetalHawk [35]. Cd tetrahedral sites of metalloproteins were retrieved from PDB [36], using the following query:

QUERY: Chemical ID(s) = CD **AND** ((Experimental Method = "X-RAY DIFFRACTION" **AND** Polymer Entity Type = "Protein") **AND** (Refinement Resolution = [0.5–1] **OR** Refinement Resolution = [1–1.5] **OR** Refinement Resolution = [1.5–2] **OR** Refinement Resolution = [2–2.5])).

Only sulfur atoms within 2.8 Å distance from Cd have been included in the final statistics.

Backbone atom coordinates from crystallographic structures of CdMETPsc1 obtained at 130 K, 160 K, 200 K and 300 K were aligned to those obtained at 100 K using the MD Analysis package and average structure coordinates were computed from the aligned models. Models at all temperatures were then aligned to the average structure and cartesian displacements were calculated for all non-hydrogen atoms from the corresponding atoms in the average structure. Overall displacement values for each temperature were computed by averaging over all residues excluding the N-terminal acetyl and C-terminal amide groups. Entropy values were calculated from the MetalHawk output vectors for structures obtained at each temperature using the probabilities assigned by the neural network for each of the seven geometry classes and the definition of Shannon entropy [35,37].

2.5. *Molecular dynamics*

Molecular Dynamics (MD) simulations have been performed using the GROMACS 2020.1 package [38] with the CHARMM36 force field, starting from the crystal structures of CdMETPsc1 solved at different temperatures (100 K, 130 K, 160 K, 200 K, 300 K). The protein was placed at the center of a dodecahedral box at a minimum distance of 1.0 nm from the box edge, and it was solvated with TIP4P water molecules (see Fig. S5 caption for details). [39,40] The system was neutralized with Na^+ ions, and electrostatics were handled via the Particle Mesh Ewald (PME) method. After energy minimization (steepest descent with convergence threshold: 100 kJ mol^{-1} nm^{-1}) the system was first equilibrated at each simulation temperature in the NVT ensemble for 1 ns using the V-rescale thermostat, then in the NPT ensemble for 1 ns using the Berendsen barostat. During both equilibration phases a positional restraints of $k = 1000$ kJ mol^{-1} nm^{-2} was applied to protein heavy atoms and a 1 fs integration time step was used. Finally, production simulations in the NPT ensemble have been performed for 100 ns each using the Parrinello–Rahman barostat, an integration time-step of 2 fs and the LINCS constraint algorithm applied to covalent bond lengths. Production at each temperature was triplicated to enhance sampling statistics. Additional simulations were performed at intermediate temperatures (180 K, 190 K, 220 K, and 250 K) to better characterize CdMETPsc1 behavior near its glass transition temperature, following the same protocol.

Cofactor bonded parameters have been calculated with quantum mechanical calculations in the framework of density functional theory (DFT), using the TURBOMOLE 4.1 suite of programs [41]. More in detail, Cd^{2+}–$S(Cys)^-$ bonded parameters, within the $[Cd(S–Cys)_4]^{2-}$ site, have been calculated through a potential energy surface scan procedure, performed at the B3LYP-D3/def2-TZVP level [42–45]. The same level of theory has been used to calculate the restrained electrostatic potential (RESP) charges of the $[Cd(S–Cys)_4]^{2-}$ site. All the parameters adopted for the $[Cd(S–Cys)_4]^{2-}$ site are reported in Fig. S5.

The above-described MD protocol has also been used to perform additional MD simulations on the zinc variant (ZnMETPsc1) and of the apo form (ApoMETPsc1) of the protein (see Fig. S6 for details).

3. Results

3.1. *CdMETPsc1 resembles Cd-substituted Rubredoxins by UV-Vis spectroscopy*

Cadmium(II) coordination by METPsc1 was followed by UV–Vis spectroscopy. When a buffered solution of METPsc1 (60 μM, 5 mM HEPES pH 7.0) was mixed with a stoichiometric amount of $CdCl_2$, a broad band centered at 240 nm appears in the spectrum (Fig. S1). This very intense band is characteristic of the S➔Cd ligand-to-metal charge transfer transition, previously observed in Cd-substituted Rd and other related proteins [46]. Molar absorptivity corresponds to ~5.3 mM^{-1} cm^{-1} per Cd—S bond, which agrees with the expected 6.0 mM^{-1} cm^{-1} (Table S1).

3.2. *CdMETPsc1 crystal is isomorphous to ZnMETPsc1 crystal*

The CdMETPsc1 crystal is isomorphous to the previously determined ZnMETPsc1 crystal [25]. The asymmetric unit of the crystal structure of CdMETPsc1 complex contains one monomer chain with a single coordinated cadmium ion. The structure of CdMETPsc1 complex displays an overall C_2–pseudosymmetrical shape resembling a truncated cone with the four Cys residues coordinating the cadmium ion located at its vertex, similar to the previously structurally characterized ZnMETPsc1.

The superposition between the crystal structures of the CdMETPsc1 (PDB ID: 9g39) complex and the ZnMETPsc1 complex (PDB ID: 5sbg) reveals a high degree of similarity, with a root-mean-square deviation (RMSD) of 0.14 Å for the 28 Cα atoms (Fig. S2A). Despite these similarities, differences are noticeable at the level of side-chain conformations, especially for the side chains exposed to the solvent, such as residues $Gln,^{11}$ and $Arg.^{28}$ Further, though most water molecules are conserved, some unique water molecules are found to interact with flexible side chains.

The crystal packing is stabilized by an intermolecular salt bridge between Arg^{26} and Asp^4 residues (Fig. S3), as well as an interaction between -OH groups of Tyr^{17} and the equivalent residue of a crystallographic-related METPsc1 molecule, much alike the previously reported zinc structure. Additionally, hydrophobic interactions pair the bottom face of the truncated cone with the lateral face exposing the type I′ β-turn. The shell around the macromolecules is hydrated, the CdMETPsc1 complex forming two topologically large channels (Fig. S3). The first central channel of larger diameter (17.5 Å) around the C-centered midpoint of the space group $C222_1$, is surrounded by negatively charged residues of Asp. The narrower second channel (14.9 Å) is formed by crystallographic binary axes and features several positively charged Arg residues. Equivalent channels were found in the isomorphous ZnMETPsc1 crystal, though slightly narrower.

3.3. *METPsc1 accomodates cadmium ion by a concerted conformational mechanism*

The Cd^{2+} coordination in METPsc1 exhibits a slightly distorted tetrahedral coordination, sulfur atoms being correlated by a D_{2d} symmetry (Fig. 2A-B), with average bond distances (2.52 ± 0.02 Å) and angles (109 ± 3°) falling within the experimental error of the average distribution found for complexes between Cd^{2+} and small molecule ligands containing sulfur atoms (Fig. 2C-D).

A comparison between the crystal structure of the METPsc1 Cd complex collected at 100 K and the cadmium-substituted *Cp*Rd (PDB ID: 1r0i) [47] reveals a striking similarity in their coordinative geometric values. This result showcases the minimal effect of a synthetic protein on a coordinatively conserved metal-sulfur cluster. Tetrahedral cadmium metal coordination in METPsc1 is similar to zinc coordination in the

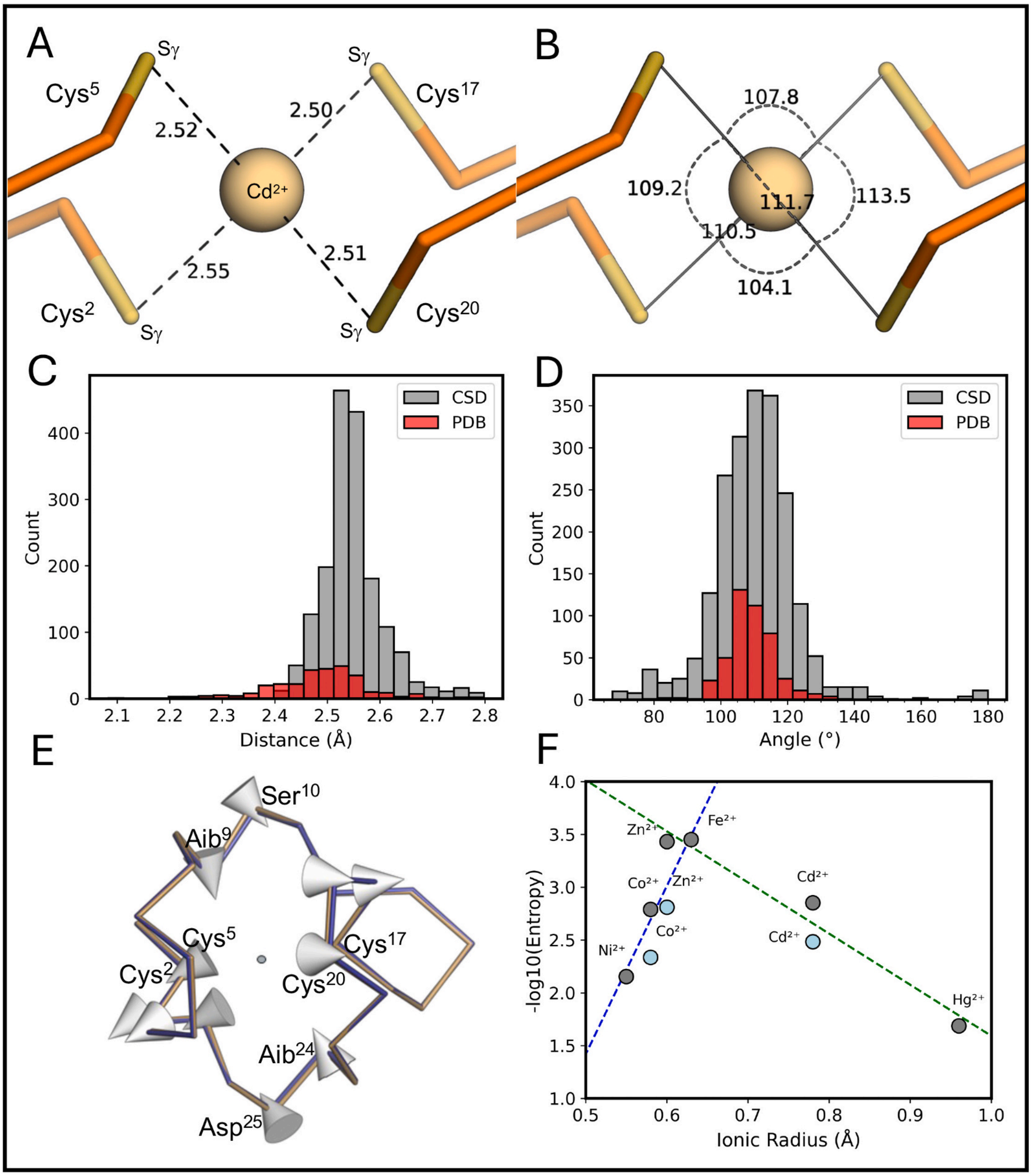

Fig. 2. Cadmium coordination geometry. Cd^{2+}—S_{γ} Distances (A, reported in Å) and S_{γ}—Cd^{2+}—S_{γ} Angles (B, reported as dashed circles between the inscribed atoms) in CdMETPsc1 structure acquired at 100 K (Cys side chains and S_{γ} are reported as orange and yellow sticks, respectively; Cd^{2+} is reported as an ochre sphere). Histogram analysis of Cd^{2+}—S bond lengths (C) and S_1—Cd^{2+}—S_2 angles (D) (small molecule complexes from the CSD and macromolecular complexes from the PDB are reported in grey and red, respectively). (E) Visualization of METPsc1 conformational rearrangement upon zinc to cadmium (PDB ID: 5sbg, 9g39, yellow and blue backbone traces, respectively) coordination. Grey cones highlight Cα atom displacements higher than 0.14 Å, considering ZnMETPsc1 as the reference frame of the trajectory. (F) MetalHawk entropy values as a function of ionic radius of the metal ion bound to either METPsc1 (cyan circles. PDB ID: Co^{2+}: 5sbi; Zn^{2+}: 5sbg; Cd^{2+}: 9g3b) or *Cp*Rd (grey circles. PDB ID: Ni^{2+}: 1r0j; Co^{2+}: 1r0h; Zn^{2+}: 1irn; Fe^{2+}: 1smw; Cd^{2+}: 1r0i; Hg^{2+}: 1r0g). Dashed lines represent trends in entropy for first row transition metals (blue line) and for 12th group metals (green line). (For interpretation of the references to colour in this figure legend, the reader is referred to the web version of this article.)

ZnMETPsc1 complex. The average bond angle in CdMETPsc1 is 109° as in ZnMETPsc1. However, the average Sγ-metal distance is ~0.2 Å shorter in ZnMETPsc1 (2.34 Å) compared to CdMETPsc1, due to the smaller radius of the zinc ion (0.74 Å) versus the cadmium ion (0.95 Å).

The shape of the coordinative tetrahedron differs between CdMETPsc1 and ZnMETPsc1. While both exhibit a clockwise distribution of Cys sidechains around the metal center (χ^1 is either g^+ or *t* for Cys^5/Cys^{20} and Cys^2/Cys^{17}, respectively), the torsion angles Sγ–Cβ (Cys^2)-Cβ–Sγ(Cys^{17}) and Sγ–Cβ(Cys^5)-Cβ–Sγ(Cys^{20}) are distinct. In CdMETPsc1, these angles are −115° and − 80°, respectively, compared to −112° and − 71° in ZnMETPsc1, thus releasing the steric hindrance due to the larger Cd^{2+} primarily by the mutual displacement of the two surface-exposed Cys residues. These values result in a more compressed tetrahedron in CdMETPsc1 along the main axis of the conical shape of the protein. Beyond first coordination shell, the whole METPsc1 scaffold undergoes a collective motion to host the second series transition metal involving the two halves of the protein. Specifically, a sliding mechanism compresses the protein along one direction, bringing the two 3_{10} helices (Aib^9-Gln^{11} and Aib^{24}-Arg^{26}) closer to each other, while it elongates the protein along the perpendicular direction, the two α-turns (Cys^2-Cys^5 and Cys^{17}-Cys^{20}) being pushed further apart (Fig. 2E). We have also analyzed the consequences of metal substitution in

C. pasteurianum rubredoxin, specifically the replacement of the zinc ion (PDB ID: 1irn) with a cadmium ion (PDB ID: 1r0i) [47,48]. This substitution results in a less symmetrical motion compared to METPsc1 (Fig. S2). The conformational changes are more pronounced near the metal-binding site, while, further away from the metal, the protein undergoes an almost negligible reorganization of the backbone. Analysis of metal site entropy, as calculated by MetalHawk [35], for different metal-substituted Rd and METPsc1 structures also supports a slightly more pronounced distortion of the latter (Fig. 2F) in response to the binding of metals different from iron. The MetalHawk entropy as a function of the ionic radius nicely captures the *Cp*Rd selectivity towards Fe^{2+} ion, clearly reflected by the volcano shape of the plot (Fig. 2F, grey circles). Though a similar dependence is observed in the case of METPsc1 (Fig. 2F, cyan circles), comparatively larger entropy values suggest a higher propensity towards distortion of the metal site to accommodate various other metal ions, most probably reflecting in a lower degree of selectivity towards a specific ionic radius. This can also be interpreted in terms of the concerted backbone reorganization, previously observed for METPsc1. In this respect, the miniaturized protein relaxes the metal site reorganization, over the whole protein thus being more adaptable to different ionic radii, differently from the more localized distortion observed in Rd. This result shows how not only the precise orientation of the metal-binding sidechains but also the dynamic behavior of the protein matrix as a whole exerts a crucial role over metal ion selectivity.

3.4. *Temperature influence on CdMETPsc1 crystal structure*

Inspired by the observations about the conformational fluidity of the METPsc1, we performed a temperature-dependent X-ray diffraction study of CdMETPsc1, ranging from 100 K to 300 K. From the data collection statistics (Table S2), the crystal showed no damage upon different data collections, including room temperature data for which the crystal was protected with paratone oil to avoid dehydration. A global temperature effect on crystal structure manifests as a dispersion in cell parameters, with an increase mainly observed in the *b* and *c* axes from 100 K to 300 K (see Table S2).

The refined models of the CdMETPsc1 complex at various temperatures generally exhibit striking similarity, as shown by the backbone calculated RMSD <0.24 Å between the various structures compared to that collected at 100 K, within the margins of the experimental error (Fig. 3A). Notably, despite these remarkable similarities over a wide temperature range, differences are noticeable among the structures, especially at the level of sidechain conformational changes for residues involved in crystallographic packing (Fig. 3A). A closer analysis of the average residue displacements as a function of the temperature shows that a significant drift from the average structure starts only after 160 K,

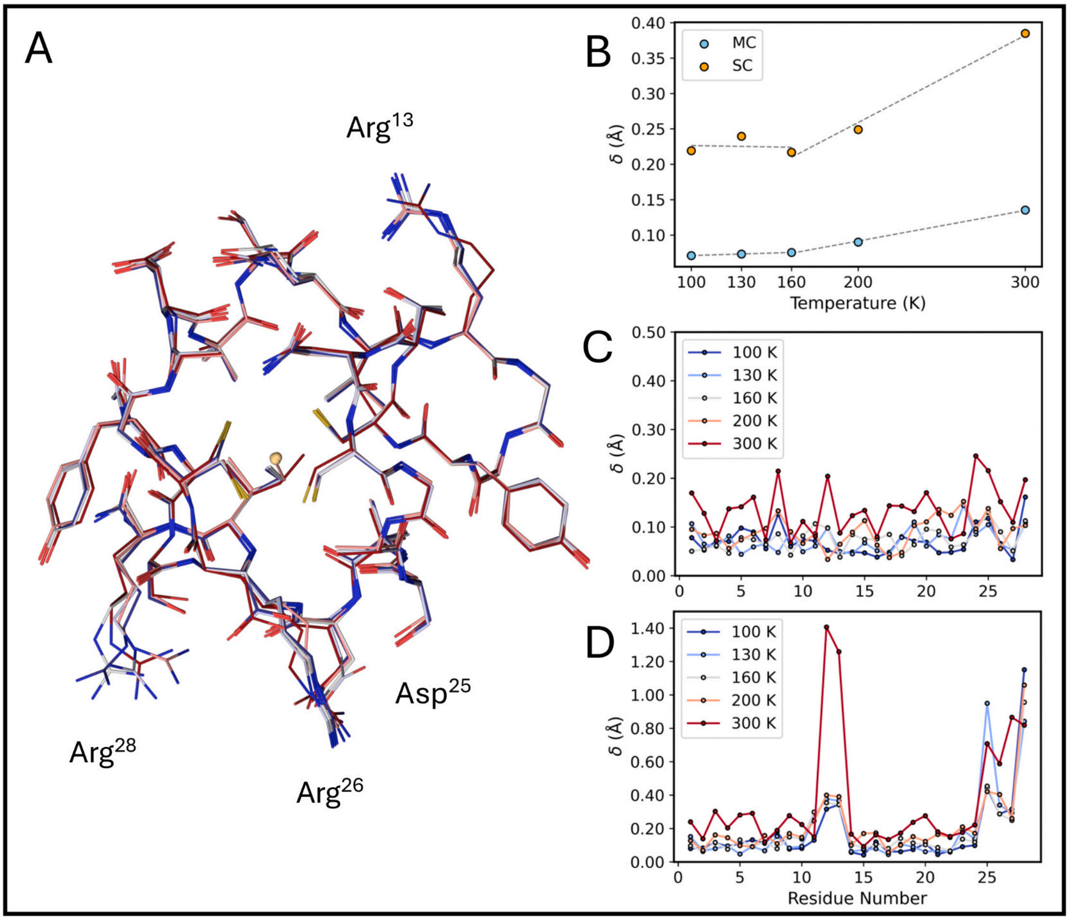

Fig. 3. Temperature influence over CdMETPsc1 crystal structure. (A) Best-fit superposition with respect to the backbone atoms of the refined models acquired at different temperatures (100 K: dark blue, 130 K: light blue, 160 K: grey, 200 K: light red, 300 K: dark red). Protein backbone/sidechains and Cd^{2+} ions are reported as sticks and ocher spheres, respectively. (B) Displacement from average structure computed over the 100–300 K temperature range for main chain atoms (MC, blue circles) and sidechain atoms (SC, orange circles). The two different trends of the data points before and after 160 K are reported as dashed lines and are intended as a guide for the eye. Detailed breakdown of displacement values from the average structure per residue for main chain (C) and sidechain (D) atoms. Increasing temperature is shown from blue to red coloration. (For interpretation of the references to colour in this figure legend, the reader is referred to the web version of this article.)

both for the main chain and the side chains (Fig. 3B).

Specifically, average per-residue displacement of the main chain is within 0.25 Å, showing only partial mobility of the backbone within this temperature range (Fig. 3C). The backbone structure is fairly rigid over the entire sequence, as no high-mobility regions emerge. Starting at 160 K, a sequence-specific correlation emerges where the C-terminal pseudo-symmetrical half of METPsc1 (residues 14–28) displays 16 % higher displacements on average (0.11 Å vs 0.09 Å) compared to its N-terminal counterpart (residues 1–13) across the 160–300 K range. On the opposite, the major displacement values for the side chains are substantially localized in the two pseudo-symmetrical related regions, corresponding to Gln^{11}-Arg^{13} and Arg^{26}-Arg^{28}, as they are involved in crystal packing or solvent interactions (Figs. 3D).

We then analyzed B-factor, also known as temperature factor values across varying temperatures to establish connections between B-factor fluctuations and temperature-induced conformational changes, as outlined in recent literature [49]. The B-factor is related to the atomic displacement by the eq. $B = 8\pi^2\chi^2$ where χ represents the mean-square atomic displacement from the average position [50,51]. Despite the well-documented recognition of B-factor dependency on temperature, dating back to Wilson's seminal reports in the 1940s, normalization approach revealed that these values are not inherently temperature-dependent [52]. The average B-factor values from refinement show the expected increase with temperature (Fig. 4).

We analyzed the change in B-factor as a function of temperature by evaluating the observed B-factor (B_{obs}) using the equation $B_{obs} = B_0 \times e\hat{}$ (kT), where B_0 represents the B-factor interpolated at zero Kelvin, k is the thermal constant, and T is the data collection temperature (Fig. 4A) [51]. The interpolation yielded a value of k equal to 0.006 K^{-1} and a B_0 value of approximately 6 $Å^2$, consistent with those observed for natural proteins, despite the relatively small size of the artificial METPsc1 protein. Furthermore, by scaling down B-factor values with the average B-factor, we derived normalized B-values (B_{norm}) using the equation $B_{norm} = B_{obs}/B_{avg}$. This analysis sheds light on intrinsic B-factor values along the METPsc1 chain, highlighting differences that are mainly influenced by intramolecular, crystallographic, or intermolecular interactions. Unlike the rather even dispersion observed for the main chain (Fig. 4B), the B_{norm} distribution for side chains shows significant changes corresponding to side chains involved in major conformational changes (Fig. 4C). Thus, this analysis offers a more direct structural insights compared to the classical analysis of B-factor values [20]. Analysis of normalized B-factors reveals distinct behaviors for specific residues. Ala^7, with its methyl group proximal to the coordinative residue Cys^{17}, shows an anomalous peak in B-factor specifically at 160 K, accompanied by weaker electron density. This observation, along with a residual Fourier map peak at 1.8 Å from its side chain, suggests localized radiation damage particularly evident in the 160 K dataset (Fig. 4B). Gln^{11} exhibits a different pattern, showing elevated B_{norm} values at lower temperatures that gradually decrease to average values as temperature increases (Fig. 4C). This behavior likely reflects temperature-dependent changes in crystal packing interactions and local solvent structure, as previously pointed out (Fig. 3D). At lower temperatures, Gln^{11} interactions with partially occupied water molecules may constrain it in specific conformations, while higher temperatures allow more uniform conformational sampling, leading to more typical B-factor values relative to the protein average.

3.5. *Cadmium-sulfur anisotropy analysis and second shell interactions*

The relatively high resolution of the METPsc1-Cd complex structures obtained at different temperatures allowed for anisotropic refinement of the heavier atoms: the cadmium ion and the four coordinating sulfur atoms (Fig. 5A). This refinement consistently improved the R_{free} values and overall refinement statistics (Table S2), offering insights into the directionality and strength of the metal-ligand interactions. Notably, analysis of cadmium-sulfur bond distances revealed an increase when comparing the 100 K structure to the 300 K structure, indicating these bonds elongate as temperature rises. This aligns with the observation of increased anisotropic motion for METPsc1 in complex with cadmium(II) at higher temperatures (Fig. 5A). The cadmium ion displays a fairly spherical anisotropy with slight elongation, in the direction of Cys^5, while the sulfur atoms exhibit greater anisotropic directionality, likely due to its involvement in the second-shell hydrogen bonding interactions.

To further inspect metal site geometry as a function of temperature, we adopted MetalHawk to evaluate tetrahedral distortion for each data collection. This can be measured as the Shannon entropy of the probability vector assigned by the model (Fig. S4). A clear temperature dependence can be observed above 130 K, as also exemplified by the anisotropy analysis. Such distortion does not seem to possess a pathway towards a specific coordination geometry because all classes get larger probabilities at higher temperatures. It can be preliminary hypothesized that positional uncertainty plays a major role in the observed trend. Nonetheless, previous analyses also suggest that at increased temperatures the fluxional protein ligand accesses more distorted average conformations.

The METPsc1 scaffold has previously been used to engineer the second coordination shell of amino acids, allowing for fine-tuning of redox potentials for various metal ions in sulfur-rich environments [25]. The second coordination shell in METPsc1 is characterized by hydrogen bonds (H-bonds) involving Cys Sγ and backbone N—H donors. In the wild-type sequence, Cys^2 accepts H-bonds from the backbone amide groups of Asp^4 and Cys^5, and the same occurs for the symmetry-related Cys^{17} (from Asn^{19} and Cys^{20} backbone amides) (Fig. 5B). Interestingly,

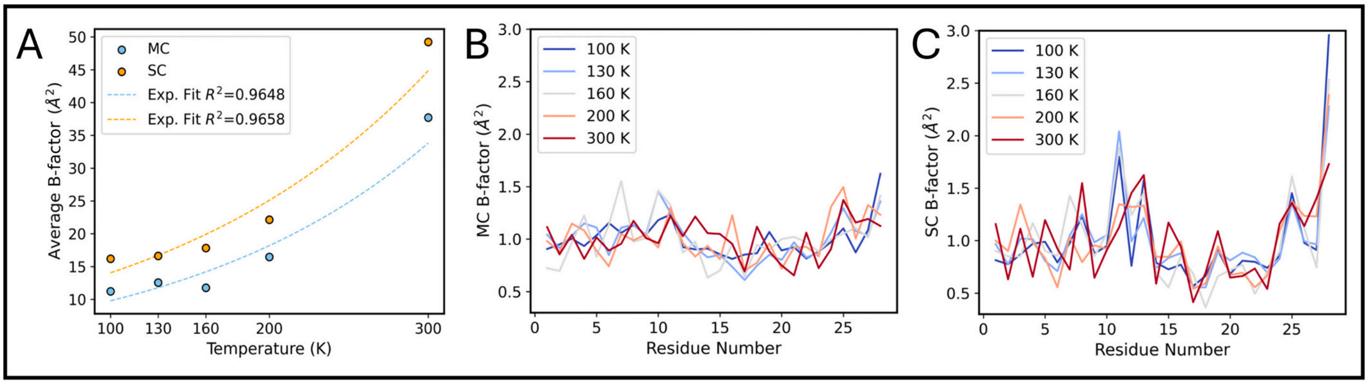

Fig. 4. Temperature induced conformational changes in CdMETPsc1. (A) Overall B-factor changes as a function of temperature for main chain (MC) and side chains (SC). (B) B-factor distribution for main chain (MC) at varying temperature. (C) B-factor distribution for side chains (SC) at varying temperature (colour scheme as in Fig. 3).

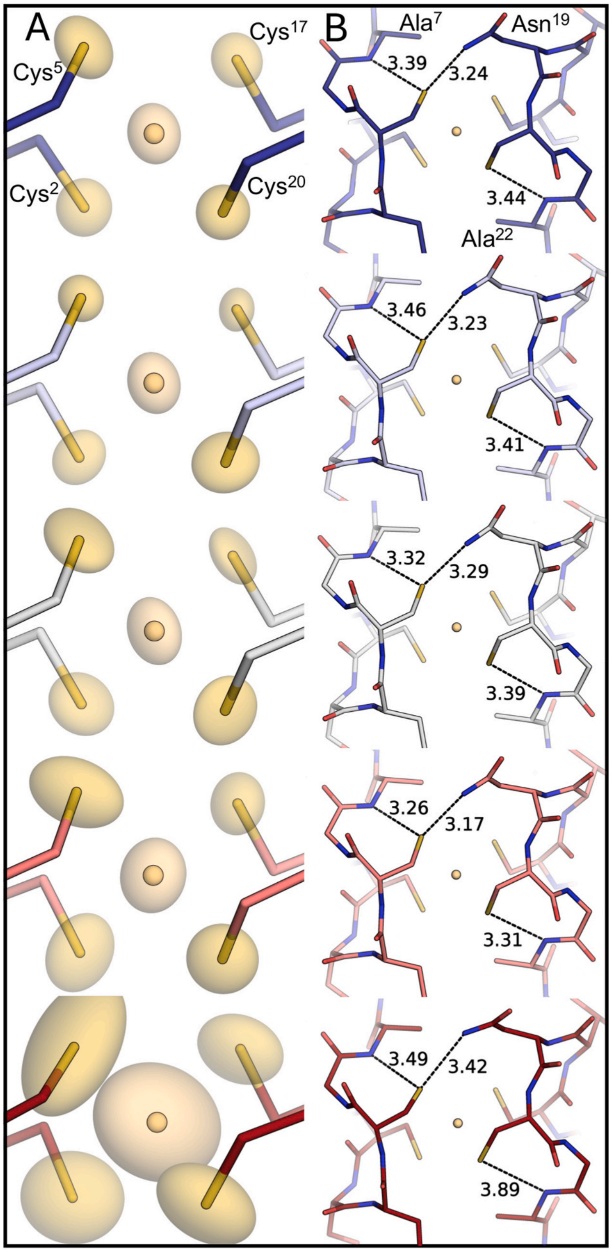

Fig. 5. First (A) and second (B) shell coordination as a function of temperature (100 K: dark blue, 130 K: light blue, 160 K: grey, 200 K: light red, 300 K: dark red, increasing from top to bottom) for CdMETPsc1 crystal structure. The metal site perspective is consistent between panels; residue labels are displayed in top panels only for clarity. Anisotropic temperature ellipsoids were evaluated for Cd^{2+} ion (ocher sphere) and S atoms and plotted as transparent yellow oblates. Hydrogen bonds involving Cys^{5} and Cys^{20} are measured and reported as black dashes. (For interpretation of the references to colour in this figure legend, the reader is referred to the web version of this article.)

the designed sequence introduces Ala residues at positions 7 and 22. These smaller residues allow their backbone N—H groups to form H-bonds with Cys^{5} and Cys^{20} Sγ, respectively. This modified second coordination sphere, formed by the amide groups of Ala^{7} and Ala^{22}, strengthens hydrogen bonding interactions with Asn^{19} and the symmetry-related Arg^{26} side chains (Fig. 5B). These second-shell interactions, conserved between the zinc and cadmium complexes of METPsc1, exhibit significant temperature dependence, particularly at room temperature, suggesting a dynamic role in protein function.

These observations agree with those observed for the natural rubredoxin. The cadmium ion in METPsc1 displays similar anisotropy to the equivalent atom in the rubredoxin-cadmium complex (PDB ID: 1r0i).

3.6. Molecular Dynamics of CdMETPsc1 in aqueous environment

The information gained on the temperature-dependent dynamic features of CdMETPsc1 in the crystal state prompted us to unravel its dynamic behavior in its physiological environment. The trend of the dynamic behavior of proteins in water solution with temperature origins, on the one hand, from protein "internal" potential energy surface, that captures the landscape of its intrinsic motion, and on the other, from perturbations caused by the solvent. To address this issue, we performed molecular dynamics (MD) simulations of CdMETPsc1 in water since MD has proved a powerful tool to investigate protein changes in flexibility going from 300 K to cryogenic-like conditions [39,53–57]. More in detail, MD simulations of CdMETPsc1 at 300 K, 200 K, 160 K, 130 K, and 100 K were done to have a direct comparison with experimental data and, to discretize more accurately (when necessary) CdMETPsc1 dynamic feature changes with temperature, we also performed MD at other intermediate temperatures. MD at 300 K suggests that CdMETPsc1 adopts a stable and equilibrated structure along the whole trajectories, as indicated by the calculated root mean square deviation (RMSD), that oscillates around 1.8 Å. Interestingly, a comparable RMSD profile was observed for ZnMETPsc1 (1.9 Å), whereas ApoMETPsc1 showed a more fluctuating RMSD profile along with a higher average value (2.6 Å). These findings highlight the crucial role of metal coordination in stabilizing METPsc1 and influencing its dynamic behavior in solution (see Fig. S6 for details).

Principal Component Analysis (PCA) indicates that the CdMETPsc1 motion captured by the first eigenvector describes the same sliding mechanism observed on the basis of METPsc1 crystal structure analysis (i.e. approach of the two Aib^{9}-Gln^{11} and Aib^{24}-Arg^{26} 3_{10} helix and distancing of the Cys^{2}-Cys^{5} and Cys^{17}-Cys^{20} turns), confirming that it is an intrinsic collective motion of the protein scaffold. At lower temperatures RMSD decreases, as expected, but higher variations in protein mobility are observed in the 300–180 K range, while in the case of temperatures below 180 K, CdMETPsc1 RMSD properties remain essentially unaltered (Fig. 6A). Similar considerations can be made by looking at root mean square fluctuations (RMSF) of both MC (Fig. 6B) and SC (Fig. 6C) of each residue. This behavior suggests the presence of a switch in CdMETPsc1 dynamics, which may be indicative of a glass-like transition. Indeed, it has been widely demonstrated that hydrating waters have a role in the manifestation of a glass transition observed in native proteins around 200 K, at which the increase of the amplitude of anharmonic motions has been correlated with an onset of protein function(s) [58–60]. To verify this aspect, we analyzed the average RMSF values (separating contributions from MC and SC) calculated in the 100–300 K range, as also done for experimental B factors (Fig. 4A). Besides the trivial observation that the increase in SC mobility with temperature is more marked than that of MC, we could observe a clear change in slope going from low temperatures to higher ones, occurring at around 185–195 K. In fact, a bilinear interpolation reproduces slightly better RMSF value distributions ($R^2 = 0.9927$–0.9899 for RMSF SC and $R^2 = 0.9786$–0.9875 for RMSF MC, Fig. 6D) rather than an exponential fit ($R^2 = 0.9811$ for RMSF SC and 0.9762 for RMSF MC). This clearly suggests that CdMETPsc1 undergoes a glass transition around 190 K in aqueous solution, just like natural proteins. Finally, we calculated normalized RMSF values (Fig. 6E, and F) as done with the experimental B factors, according to the formula $RMSF_{norm} = RMSF_{obs}/RMS_{avg}$, where $RMSF_{obs}$ is referred to the calculated RMSF value for each residue averaged over the replicas. Doing so, we could better appreciate changes in the intrinsic flexibility of both MC and SC among different temperatures, also allowing a comparison between protein dynamics in solution and in crystal state. $RMSF_{norm}$ variability along the protein sequence tends to progressively decrease going from 300 K to 100 K, and, in

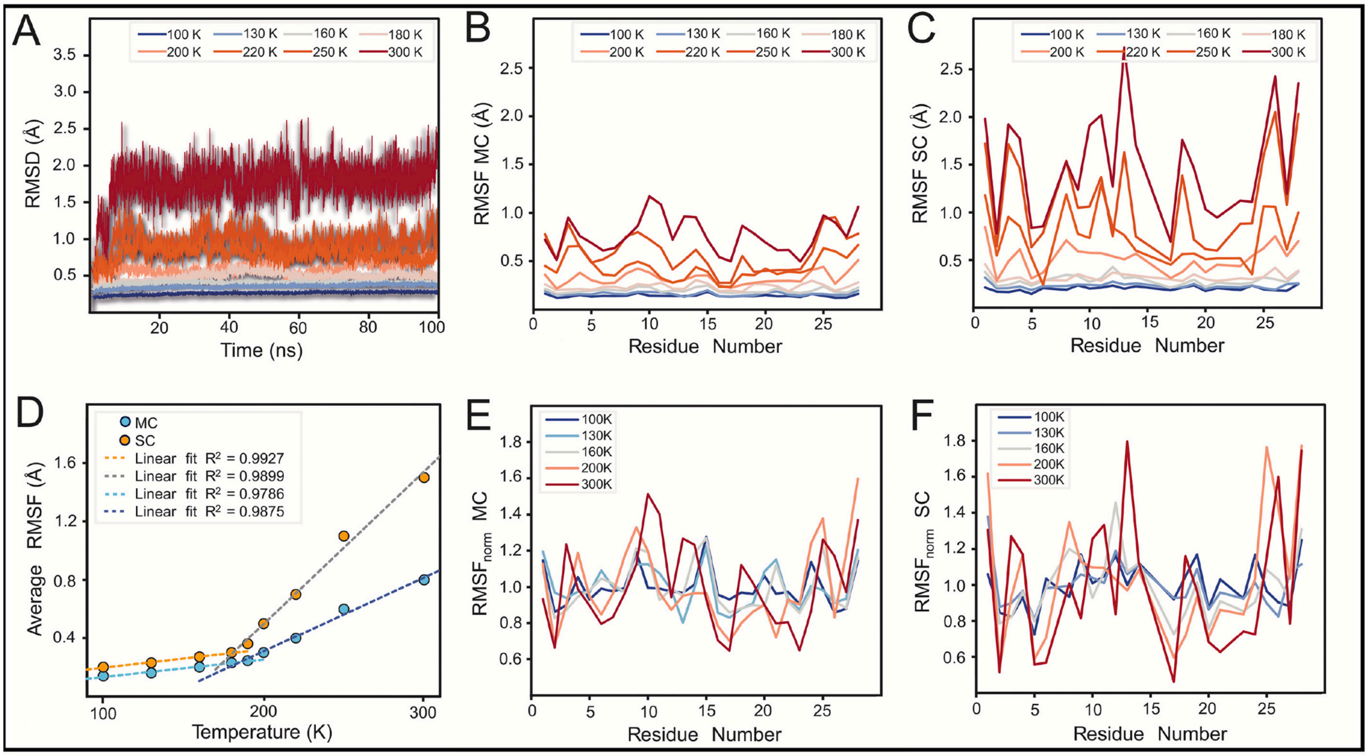

Fig. 6. Backbone RMSD (A), main chain RMSF (B) and side chain RMSF (C) analysis for CdMETPsc1 100 ns MD trajectories at different temperatures; Temperature dependence of the average main chain RMSF and side chain RMSF values (D); Normalized RMSF values for main chain (E) and for side chain (F) calculated at different temperatures (colour scheme as in Fig. 3).

accordance with B_{norm} analysis, $RMSF_{norm}$ MC values are more leveled than those calculated for side chains, underlying the expected higher flexibility of the latter, irrespective of temperature and protein environment. In general, the flexibility patterns calculated for in-solution CdMETPsc1 qualitatively resemble those obtained for the crystal state, but with some deviations.

For instance, side chains in the Glu^{11}-Arg^{13} and Arg^{26}-Arg^{28} are associated with the highest $RMSF_{norm}$ values, in line with the observed B factor, but we could also notice a significant mobility in the N-terminal region side chains (except for Cys), indicating that the dynamics of CdMEPTsc1 varies to some extent in aqueous environment.

4. Discussion

The field of protein design, propelled by rapid advancements in computational chemistry, is poised to revolutionize biotechnology [61–63]. Our study of METPsc1, a miniaturized electron transfer protein, exemplifies the potential of this approach while highlighting the complexities involved in designing functional protein-metal complexes. The comprehensive characterization of CdMETPsc1 across a wide temperature range offers valuable insights into the interplay between protein structure, dynamics, and function within a designed protein.

Our findings reveal that METPsc1 exhibits a remarkable ability to optimize its ligand shell in response to divalent cations of varying radii, mirroring the adaptability observed in natural rubredoxins. This flexibility is facilitated by a unique "clothespin-like" recoil mechanism of the protein backbone, as evidenced by our temperature-dependent analysis. The subtle temperature-dependent shifts in side-chain conformations, particularly for residues involved in crystal packing, highlight the dynamic nature of protein-metal interactions. The temperature-dependent behavior of second-shell hydrogen bonding interactions, notably those involving Ala^{7}/Ala^{22} and Asn^{19}/Arg^{26}, suggests a dynamic role in modulating protein function. These findings underscore the importance of considering both first and second coordination spheres in the design of metalloprotein mimics [4,64].

This dynamic behavior allows the protein to accommodate changes in metal ion radius, a crucial feature for maintaining stability during redox cycles, though the scaffold must be stable enough to accommodate and absorb throughout its entire structure the changes happening in the proximity of the metal cofactor [65–67], as we showed in the displacement analysis upon ion substitution for both METPsc1 and natural Rd. The observed mechanism may explain why simpler dimeric analogues previously synthesized were unable to withstand multiple redox cycles [68,69], underscoring the importance of protein scaffold design in metal coordination. The recoil mechanism observed in METPsc1 can also be interpreted through the lens of the entatic state concept, particularly in the context of the radius change accompanying the Fe(II)/Fe(III) redox transition. The protein's ability to adapt its coordination environment suggests a design that effectively balances the conflicting requirements of different oxidation states, a hallmark of efficient electron transfer proteins. This finding not only validates our design approach but also offers insights into the fundamental principles governing electron transfer in metalloproteins.

Our temperature-dependent X-ray diffraction studies, particularly those conducted at room temperature, provide a more physiologically relevant view of protein dynamics [20]. The analysis of B-factors across different temperatures allowed us to distinguish between vibrational motion and static disorder, offering a nuanced understanding of protein flexibility. The observed increase in relative flexibility around the metal-binding site at higher temperatures aligns with findings from studies on psychrophilic enzymes, suggesting a potential link between flexibility and function [70,71]. Moreover, our room-temperature data revealed conformational substates that may be crucial for metal binding and redox cycling, which are often obscured in cryo-cooled structures [23].

The observed anisotropic behavior of the sulfur atoms involved in second-shell hydrogen bonding, coupled with the lengthening of Cd—S bonds at higher temperatures, provides insight into the dynamic interplay between the metal center and the protein scaffold. This temperature-dependent behavior may be crucial for fine-tuning the protein's redox properties and could be exploited in future designs to create metalloproteins with tailored functionalities.

In conclusion, our comprehensive analysis of CdMETPsc1 across a range of temperatures provides valuable insights into the principles governing protein-metal interactions and, implicitly, electron transfer processes. The observed dynamic adaptability of METPsc1 validates our design approach and offers a blueprint for creating more efficient and stable metalloproteins. Future work should focus on leveraging these insights to design proteins with enhanced functional properties, potentially leading to novel catalysts and sensors with applications in biotechnology and environmental remediation. Moreover, this specific protein-metal complex holds potential for future applications, such as the development of catalysts for quantum CdS dots or bioremediation strategies to extract cadmium from toxic environments [72,73]. It is well-documented that cadmium exposure represents a ubiquitous environmental contamination.

CRediT authorship contribution statement

Luigi F. Di Costanzo: Writing – review & editing, Writing – original draft, Validation, Investigation, Formal analysis, Data curation, Conceptualization. **Gianmattia Sgueglia:** Writing – review & editing, Formal analysis, Data curation. **Carla Orlando:** Formal analysis, Data curation. **Maurizio Polentarutti:** Resources, Investigation, Data curation. **Linda Leone:** Writing – review & editing, Investigation, Formal analysis. **Salvatore La Gatta:** Investigation, Writing – review & editing. **Maria De Fenza:** Writing – review & editing, Visualization. **Luca De Gioia:** Writing – review & editing, Project administration, Funding acquisition. **Angela Lombardi:** Writing – review & editing, Project administration, Funding acquisition. **Federica Arrigoni:** Writing – review & editing, Writing – original draft, Investigation, Funding acquisition, Formal analysis. **Marco Chino:** Writing – review & editing, Writing – original draft, Supervision, Funding acquisition, Formal analysis, Conceptualization.

Declaration of competing interest

The authors declare that they have no known competing financial interests or personal relationships that could have appeared to influence the work reported in this paper.

Data availability

The atomic coordinates and structure factors for all temperature-dependent X-ray crystallographic data have been deposited in the Protein Data Bank (https://www.rcsb.org) under accession numbers: 9g39 (100*K*), 9g3bG3B (130*K*), 9g3a (160 K), 9g3c (200*K*), and 9g3u (300*K*). Molecular dynamics simulation data, including input files, parameters, and trajectories, are available at Zenodo (doi:https://doi.org/10.5281/zenodo.14209644). All other data supporting the findings of this study are available in the main text or the supplementary materials and will be made available on request.

Acknowledgements

We acknowledge financial support under the National Recovery and Resilience Plan (NRRP), Mission 4, Component 2, Investment 1.1, Call for tender No. 1409 published on 14.9.2022 by the Italian Ministry of University and Research (MUR), funded by the European Union – NextGenerationEU – Project Title "SMARFeS: Small Molecule Activation by Redesigned iron-sulfur (FeS) proteins" – CUP H53D23007950001, E53D23016070001 - Grant Assignment Decree No. 1384 adopted on 01/09/2023 by the Italian Ministry of Ministry of University and Research (MUR). We also acknowledge financial support under the National Recovery and Resilience Plan (NRRP), Mission 4, Component 2, Investment 1.3, theme 2.a "Green Energies for the Future", funded by the European Union – NextGenerationEU – Project Title "NEST – Network 4 Energy Sustainable Transition" – CUP E63C22002160007. We wish to thank Elettra Sincrotone Trieste for providing access to its synchrotron radiation facilities. M.D.F. is grateful to the Italian MUR for being granted a research fellow position (PONR&I 2014–2020, CUP E65F21003010003). L.L. is grateful to the European Research Council (ERC) for being granted a research fellow position in the frame of the "BioDisOrder" project (UGOV 000005_HORIZON2020_ERC_2018_BioDisOrder, Grant/Award Number: E64I19002960006). We are also indebted to Prof. Vincenzo Pavone for his invaluable guidance in the first steps of crystal structure determination.

Appendix A. Supplementary data

Supplementary data to this article can be found online at https://doi.org/10.1016/j.jinorgbio.2024.112810.

References

[1] T. Kortemme, De novo protein design—from new structures to programmable functions, Cell 187 (2024) 526–544, https://doi.org/10.1016/j.cell.2023.12.028.

[2] R.A. Chica, N. Ferruz, What does it take for an 'AlphaFold moment' in functional protein engineering and design? Nat. Biotechnol. 42 (2024) 173–174, https://doi.org/10.1038/s41587-023-02120-z.

[3] J.L. Watson, D. Juergens, N.R. Bennett, B.L. Trippe, J. Yim, H.E. Eisenach, W. Ahern, A.J. Borst, R.J. Ragotte, L.F. Milles, B.I.M. Wicky, N. Hanikel, S. J. Pellock, A. Courbet, W. Sheffler, J. Wang, P. Venkatesh, I. Sappington, S. V. Torres, A. Lauko, V. De Bortoli, E. Mathieu, S. Ovchinnikov, R. Barzilay, T. S. Jaakkola, F. DiMaio, M. Baek, D. Baker, De novo design of protein structure and function with RFdiffusion, Nature 620 (2023) 1089–1100, https://doi.org/10.1038/s41586-023-06415-8.

[4] A. Lombardi, F. Pirro, O. Maglio, M. Chino, W.F. DeGrado, De novo Design of Four-Helix Bundle Metalloproteins: one scaffold, diverse Reactivities, Acc. Chem. Res. 52 (2019) 1148–1159, https://doi.org/10.1021/acs.accounts.8b00674.

[5] F. Nastri, D. D'Alonzo, L. Leone, G. Zambrano, V. Pavone, A. Lombardi, Engineering Metalloprotein functions in designed and native scaffolds, Trends Biochem. Sci. 44 (2019) 1022–1040, https://doi.org/10.1016/j.tibs.2019.06.006.

[6] R. Pearce, X. Huang, G.S. Omenn, Y. Zhang, De novo protein fold design through sequence-independent fragment assembly simulations, Proc. Natl. Acad. Sci. 120 (2023) e2208275120, https://doi.org/10.1073/pnas.2208275120.

[7] K. Tsuboyama, J. Dauparas, J. Chen, E. Laine, Y. Mohseni Behbahani, J. J. Weinstein, N.M. Mangan, S. Ovchinnikov, G.J. Rocklin, Mega-scale experimental analysis of protein folding stability in biology and design, Nature 620 (2023) 434–444, https://doi.org/10.1038/s41586-023-06328-6.

[8] F. Pirro, S. La Gatta, F. Arrigoni, A. Famulari, O. Maglio, P. Del Vecchio, M. Chiesa, L. De Gioia, L. Bertini, M. Chino, F. Nastri, A. Lombardi, A De novo-designed type 3 copper protein Tunes catechol substrate recognition and reactivity, Angew. Chem. Int. Ed. 62 (2023) e202211552, https://doi.org/10.1002/anie.202211552.

[9] M. Chino, S. La Gatta, L. Leone, M. De Fenza, A. Lombardi, V. Pavone, O. Maglio, Dye Decolorization by a miniaturized peroxidase Fe-MimochromeVI*a, Int. J. Mol. Sci. 24 (2023) 11070, https://doi.org/10.3390/ijms241311070.

[10] D. D'Alonzo, M. De Fenza, V. Pavone, A. Lombardi, F. Nastri, Selective oxidation of Halophenols catalyzed by an artificial miniaturized peroxidase, Int. J. Mol. Sci. 24 (2023) 8058, https://doi.org/10.3390/ijms24098058.

[11] A. Tebo, A. Quaranta, V.L. Pecoraro, A. Aukauloo, Enhanced Photoinduced Electron transfer through a tyrosine relay in a De novo designed protein scaffold bearing a Photoredox unit and a FeIIS4 site, ChemPhotoChem 5 (2021) 665–668, https://doi.org/10.1002/cptc.202100014.

[12] F. Pirro, N. Schmidt, J. Lincoff, Z.X. Widel, N.F. Polizzi, L. Liu, M.J. Therien, M. Grabe, M. Chino, A. Lombardi, W.F. DeGrado, Allosteric cooperation in a de novo-designed two-domain protein, Proc. Natl. Acad. Sci. 117 (2020) 33246–33253, https://doi.org/10.1073/pnas.2017062117.

[13] R. Matsumoto, S. Yoshioka, M. Yuasa, Y. Morita, G. Kurisu, N. Fujieda, An artificial metallolyase with pliable 2-His-1-carboxylate facial triad for stereoselective Michael addition, Chem. Sci. 14 (2023) 3932–3937, https://doi.org/10.1039/D2SC06809E.

[14] S. Kato, M. Abe, H. Gröger, T. Hayashi, Reconstitution of myoglobin with Iron Porphycene generates an artificial Aldoxime dehydratase with expanded catalytic activities, ACS Catal. (2024) 13081–13087, https://doi.org/10.1021/acscatal.4c03220.

[15] A.G. Tebo, T.B.J. Pinter, R. García-Serres, A.L. Speelman, C. Tard, O. Sénéque, G. Blondin, J.-M. Latour, J. Penner-Hahn, N. Lehnert, V.L. Pecoraro, Development of a Rubredoxin-type center embedded in a de De novo-designed three-Helix bundle, Biochemistry 57 (2018) 2308–2316, https://doi.org/10.1021/acs.biochem.8b00091.

[16] S.I. Mann, A. Nayak, G.T. Gassner, M.J. Therien, W.F. DeGrado, De novo design, solution characterization, and crystallographic structure of an Abiological Mn–porphyrin-binding protein capable of stabilizing a Mn(V) species, J. Am. Chem. Soc. 143 (2021) 252–259, https://doi.org/10.1021/jacs.0c10136.

[17] W.C. Pitts, A. Deb, J.E. Penner-Hahn, V.L. Pecoraro, Revving up a designed copper nitrite reductase using noncoded active site ligands, ACS Catal. (2024) 4362–4368, https://doi.org/10.1021/acscatal.3c06159.

[18] A.S. Klein, F. Leiss-Maier, R. Mühlhofer, B. Boesen, G. Mustafa, H. Kugler, C. Zeymer, A De novo Metalloenzyme for cerium Photoredox catalysis, J. Am. Chem. Soc. (2024), https://doi.org/10.1021/jacs.4c04618.

[19] J. Timm, D.H. Pike, J.A. Mancini, A.M. Tyryshkin, S. Poudel, J.A. Siess, P. M. Molinaro, J.J. McCann, K.M. Waldie, R.L. Koder, P.G. Falkowski, V. Nanda, Design of a minimal di-nickel hydrogenase peptide, Sci. Adv. 9 (2023) eabq1990, https://doi.org/10.1126/sciadv.abq1990.

[20] Z. Sun, Q. Liu, G. Qu, Y. Feng, M.T. Reetz, Utility of B-factors in protein science: interpreting rigidity, flexibility, and internal motion and engineering Thermostability, Chem. Rev. 119 (2019) 1626–1665, https://doi.org/10.1021/acs.chemrev.8b00290.

[21] G. Balendiran, J. Pandian, E. Drake, A. Vinayak, M. Verma, D. Cascio, B-factor analysis and conformational rearrangement of aldose reductase, Curr. Proteomics 11 (2014) 151–160, https://doi.org/10.2174/157016461103140922163444.

[22] K.A. Henzler-Wildman, M. Lei, V. Thai, S.J. Kerns, M. Karplus, D. Kern, A hierarchy of timescales in protein dynamics is linked to enzyme catalysis, Nature 450 (2007) 913–916, https://doi.org/10.1038/nature06407.

[23] J.S. Fraser, H. Van Den Bedem, A.J. Samelson, P.T. Lang, J.M. Holton, N. Echols, T. Alber, Accessing protein conformational ensembles using room-temperature X-ray crystallography, Proc. Natl. Acad. Sci. 108 (2011) 16247–16252, https://doi.org/10.1073/pnas.1111325108.

[24] A. Ebrahim, B.T. Riley, D. Kumaran, B. Andi, M.R. Fuchs, S. McSweeney, D. A. Keedy, The temperature-dependent conformational ensemble of SARS-CoV-2 main protease (M ^{pro}), IUCrJ 9 (2022) 682–694, https://doi.org/10.1107/S2052252522007497.

[25] M. Chino, L.F. Di Costanzo, L. Leone, S. La Gatta, A. Famulari, M. Chiesa, A. Lombardi, V. Pavone, Designed Rubredoxin miniature in a fully artificial electron chain triggered by visible light, Nat. Commun. 14 (2023) 2368, https://doi.org/10.1038/s41467-023-37941-8.

[26] J. Meyer, J.-M. Moulis, Rubredoxin, in: Handb. Met, John Wiley & Sons, Ltd, 2006, https://doi.org/10.1002/0470028637.met135.

[27] B.K. Maiti, R.M. Almeida, I. Moura, J.J.G. Moura, Rubredoxins derivatives: simple Sulphur-rich coordination metal sites and its relevance for biology and chemistry, Coord. Chem. Rev. 352 (2017) 379–397, https://doi.org/10.1016/j.ccr.2017.10.001.

[28] J.W. Slater, S.C. Marguet, M.E. Gray, H.A. Monaco, M. Sotomayor, H.S. Shafaat, Power of the secondary sphere: modulating hydrogenase activity in nickel-substituted Rubredoxin, ACS Catal. 9 (2019) 8928–8942, https://doi.org/10.1021/acscatal.9b01720.

[29] W. Kabsch, XDS, Acta Crystallogr. Sect. D Biol. Crystallogr. 66 (2010) 125–132, https://doi.org/10.1107/S0907444909047337.

[30] P.R. Evans, An introduction to data reduction: space-group determination, scaling and intensity statistics, Acta Crystallogr. Sect. D Biol. Crystallogr. 67 (2011) 282–292, https://doi.org/10.1107/S090744491003982X.

[31] W. Clegg, in: W. Clegg, A.J. Blake, J.M. Cole, J.S.O. Evans, P. Main, S. Parsons, D. J. Watkin (Eds.), Fourier syntheses, Cryst. Struct. Anal. Princ. Pract, Oxford University Press, 2009, p. 0. https://doi.org/10.1093/acprof:oso/9780199219469.003.0008.

[32] D. Liebschner, P.V. Afonine, M.L. Baker, G. Bunkóczi, V.B. Chen, T.I. Croll, B. Hintze, L.-W. Hung, S. Jain, A.J. McCoy, N.W. Moriarty, R.D. Oeffner, B.K. Poon, M.G. Prisant, R.J. Read, J.S. Richardson, D.C. Richardson, M.D. Sammito, O. V. Sobolev, D.H. Stockwell, T.C. Terwilliger, A.G. Urzhumtsev, L.L. Videau, C. J. Williams, P.D. Adams, Macromolecular structure determination using X-rays, neutrons and electrons: recent developments in *Phenix*, Acta Crystallogr. Sect. D Biol. Crystallogr. 75 (2019) 861–877, https://doi.org/10.1107/S2059798319011471.

[33] P. Emsley, B. Lohkamp, W.G. Scott, K. Cowtan, Features and development of Coot, Acta Crystallogr. Sect. D Biol. Crystallogr. 66 (2010) 486–501, https://doi.org/10.1107/S0907444910007493.

[34] C.R. Groom, I.J. Bruno, M.P. Lightfoot, S.C. Ward, The Cambridge structural database, Acta Crystallogr. Sect. B Struct. Sci. Cryst. Eng. Mater. 72 (2016) 171–179, https://doi.org/10.1107/S2052520616003954.

[35] G. Sgueglia, M.D. Vrettas, M. Chino, A. De Simone, A. Lombardi, MetalHawk: enhanced classification of metal coordination geometries by artificial neural networks, J. Chem. Inf. Model. 64 (2024) 2356–2367, https://doi.org/10.1021/acs.jcim.3c00873.

[36] C. Markosian, L. Di Costanzo, M. Sekharan, C. Shao, S.K. Burley, C. Zardecki, Analysis of impact metrics for the protein data Bank, Sci. Data 5 (2018) 180212, https://doi.org/10.1038/sdata.2018.212.

[37] C.E. Shannon, A mathematical theory of communication, Bell Syst. Tech. J. 27 (1948) 379–423, https://doi.org/10.1002/j.1538-7305.1948.tb01338.x.

[38] S. Pronk, S. Páll, R. Schulz, P. Larsson, P. Bjelkmar, R. Apostolov, M.R. Shirts, J. C. Smith, P.M. Kasson, D. Van Der Spoel, B. Hess, E. Lindahl, GROMACS 4.5: a high-throughput and highly parallel open source molecular simulation toolkit, Bioinformatics 29 (2013) 845–854, https://doi.org/10.1093/bioinformatics/btt055.

[39] M. Gupta, C. Chakravarty, S. Bandyopadhyay, Sensitivity of protein glass transition to the choice of water model, J. Chem. Theory Comput. 12 (2016) 5643–5655, https://doi.org/10.1021/acs.jctc.6b00825.

[40] C. Vega, J.L.F. Abascal, M.M. Conde, J.L. Aragones, What ice can teach us about water interactions: a critical comparison of the performance of different water models, Faraday Discuss. 141 (2009) 251–276, https://doi.org/10.1039/B805531A.

[41] R. Ahlrichs, M. Bär, M. Häser, H. Horn, C. Kölmel, Electronic structure calculations on workstation computers: the program system turbomole, Chem. Phys. Lett. 162 (1989) 165–169, https://doi.org/10.1016/0009-2614(89)85118-8.

[42] A.D. Becke, Density-functional exchange-energy approximation with correct asymptotic behavior, Phys. Rev. A 38 (1988) 3098–3100, https://doi.org/10.1103/PhysRevA.38.3098.

[43] C. Lee, W. Yang, R.G. Parr, Development of the Colle-Salvetti correlation-energy formula into a functional of the electron density, Phys. Rev. B 37 (1988) 785–789, https://doi.org/10.1103/PhysRevB.37.785.

[44] S. Grimme, J. Antony, S. Ehrlich, H. Krieg, A consistent and accurate *ab initio* parametrization of density functional dispersion correction (DFT-D) for the 94 elements H-Pu, J. Chem. Phys. 132 (2010) 154104, https://doi.org/10.1063/1.3382344.

[45] F. Weigend, R. Ahlrichs, Balanced basis sets of split valence, triple zeta valence and quadruple zeta valence quality for H to Rn: design and assessment of accuracy, Phys. Chem. Chem. Phys. 7 (2005) 3297, https://doi.org/10.1039/b508541a.

[46] C.J. Henehan, D.L. Pountney, M. Vašák, O. Zerbe, Identification of cysteine ligands in metalloproteins using optical and NMR spectroscopy: cadmium-substituted rubredoxin as a model [cd(CysS)4]2- center, Protein Sci. 2 (1993) 1756–1764, https://doi.org/10.1002/pro.5560021019.

[47] M. Maher, M. Cross, M.C.J. Wilce, J.M. Guss, A.G. Wedd, Metal-substituted derivatives of the rubredoxin from *clostridium pasteurianum*, Acta Crystallogr. Sect. D Biol. Crystallogr. 60 (2004) 298–303, https://doi.org/10.1107/S090744490302794X.

[48] Z. Dauter, K.S. Wilson, L.C. Sieker, J.M. Moulis, J. Meyer, Zinc- and iron-rubredoxins from clostridium pasteurianum at atomic resolution: a high-precision model of a ZnS4 coordination unit in a protein, Proc. Natl. Acad. Sci. 93 (1996) 8836–8840, https://doi.org/10.1073/pnas.93.17.8836.

[49] F. De Sá Ribeiro, L.M.T.R. Lima, Linking B-factor and temperature-induced conformational transition, Biophys. Chem. 298 (2023) 107027, https://doi.org/10.1016/j.bpc.2023.107027.

[50] C. Giacovazzo, H.L. Monaco, G. Artioli, D. Viterbo, M. Milanesio, G. Gilli, P. Gilli, G. Zanotti, G. Ferraris, M. Catti, Fundamentals of crystallography, Oxford University Press (2011), https://doi.org/10.1093/acprof:oso/9780199573653.001.0001.

[51] P.A. Karplus, G.E. Schulz, Prediction of chain flexibility in proteins: a tool for the selection of peptide antigens, Naturwissenschaften 72 (1985) 212–213, https://doi.org/10.1007/BF01195768.

[52] A.J.C. Wilson, Determination of absolute from relative X-ray intensity data, Nature 150 (1942) 152, https://doi.org/10.1038/150152a0.

[53] J.A. Hayward, J.C. Smith, Temperature dependence of protein dynamics: computer simulation analysis of neutron scattering properties, Biophys. J. 82 (2002) 1216–1225, https://doi.org/10.1016/S0006-3495(02)75478-7.

[54] P.J. Steinbach, B.R. Brooks, Protein hydration elucidated by molecular dynamics simulation, Proc. Natl. Acad. Sci. 90 (1993) 9135–9139, https://doi.org/10.1073/pnas.90.19.9135.

[55] J. Smith, K. Kuczera, M. Karplus, Dynamics of myoglobin: comparison of simulation results with neutron scattering spectra, Proc. Natl. Acad. Sci. 87 (1990) 1601–1605, https://doi.org/10.1073/pnas.87.4.1601.

[56] D. Vitkup, D. Ringe, G.A. Petsko, M. Karplus, Solvent mobility and the protein "glass" transition, Nat. Struct. Biol. 7 (2000) 34–38, https://doi.org/10.1038/71231.

[57] A.L. Tournier, J. Xu, J.C. Smith, Translational hydration water dynamics drives the protein glass transition, Biophys. J. 85 (2003) 1871–1875, https://doi.org/10.1016/S0006-3495(03)74614-1.

[58] V.N. Morozov, S.G. Gevorkian, Low-temperature glass transition in proteins, Biopolymers 24 (1985) 1785–1799, https://doi.org/10.1002/bip.360240909.

[59] D. Ringe, G.A. Petsko, The 'glass transition' in protein dynamics: what it is, why it occurs, and how to exploit it, Biophys. Chem. 105 (2003) 667–680, https://doi.org/10.1016/S0301-4622(03)00096-6.

[60] N. Shinyashiki, W. Yamamoto, A. Yokoyama, T. Yoshinari, S. Yagihara, R. Kita, K. L. Ngai, S. Capaccioli, Glass transitions in aqueous solutions of protein (bovine serum albumin), J. Phys. Chem. B 113 (2009) 14448–14456, https://doi.org/10.1021/jp905511w.

[61] A.E. Chu, T. Lu, P.-S. Huang, Sparks of function by de novo protein design, Nat. Biotechnol. 42 (2024) 203–215, https://doi.org/10.1038/s41587-024-02133-2.

[62] L. Leone, G. Sgueglia, S. La Gatta, M. Chino, F. Nastri, A. Lombardi, Enzymatic and bioinspired Systems for Hydrogen Production, Int. J. Mol. Sci. 24 (2023) 8605, https://doi.org/10.3390/ijms24108605.

[63] M.J. Chalkley, S.I. Mann, W.F. DeGrado, De novo metalloprotein design, Nat. Rev. Chem. 6 (2022) 31–50, https://doi.org/10.1038/s41570-021-00339-5.

[64] F. Yu, V.M. Cangelosi, M.L. Zastrow, M. Tegoni, J.S. Plegaria, A.G. Tebo, C. S. Mocny, L. Ruckthong, H. Qayyum, V.L. Pecoraro, Protein design: toward functional Metalloenzymes, Chem. Rev. 114 (2014) 3495–3578, https://doi.org/10.1021/cr400458x.

[65] T. Dudev, C. Lim, Metal binding affinity and selectivity in Metalloproteins: insights from computational studies, Annu. Rev. Biophys. 37 (2008) 97–116, https://doi.org/10.1146/annurev.biophys.37.032807.125811.

[66] S.E.J. Bowman, J. Bridwell-Rabb, C.L. Drennan, Metalloprotein crystallography: more than a structure, Acc. Chem. Res. 49 (2016) 695–702, https://doi.org/10.1021/acs.accounts.5b00538.

[67] T.C. Pochapsky, S.S. Pochapsky, What your crystal structure will not tell you about enzyme function, Acc. Chem. Res. 52 (2019) 1409–1418, https://doi.org/10.1021/acs.accounts.9b00066.

[68] A. Lombardi, D. Marasco, O. Maglio, L. Di Costanzo, F. Nastri, V. Pavone, Miniaturized metalloproteins: application to iron–sulfur proteins, Proc. Natl. Acad. Sci. 97 (2000) 11922–11927, https://doi.org/10.1073/pnas.97.22.11922.

[69] S. La Gatta, L. Leone, O. Maglio, M. De Fenza, F. Nastri, V. Pavone, M. Chino, A. Lombardi, Unravelling the structure of the tetrahedral metal-binding site in METP3 through an experimental and computational approach, Molecules 26 (2021) 5221, https://doi.org/10.3390/molecules26175221.

[70] S.-Y. Kim, K.Y. Hwang, S.-H. Kim, H.-C. Sung, Y.S. Han, Y. Cho, Structural basis for cold adaptation: sequence, biochemical properties, and crystal structure of malate dehydrogenase from a Psychrophile Aquaspirillium Arcticum, J. Biol. Chem. 274 (1999) 11761–11767, https://doi.org/10.1074/jbc.274.17.11761.

[71] A. Merlino, I.R. Krauss, I. Castellano, E.D. Vendittis, B. Rossi, M. Conte, A. Vergara, F. Sica, Structure and flexibility in cold-adapted iron superoxide dismutases: the case of the enzyme isolated from *Pseudoalteromonas haloplanktis*, J. Struct. Biol. 172 (2010) 343–352, https://doi.org/10.1016/j.jsb.2010.08.008.

[72] H. Guo, R. Hu, G. Huang, W. Pu, X. Chu, C. Xing, C. Zhang, Molybdenum and cadmium co-exposure induces endoplasmic reticulum stress-mediated apoptosis by Th1 polarization in Shaoxing duck (Anas platyrhyncha) spleens, Chemosphere 298 (2022) 134275, https://doi.org/10.1016/j.chemosphere.2022.134275.

[73] H. Horiguchi, E. Oguma, S. Sasaki, K. Miyamoto, Y. Ikeda, M. Machida, F. Kayama, Dietary exposure to cadmium at close to the current provisional tolerable weekly intake does not affect renal function among female Japanese farmers, Environ. Res. 95 (2004) 20–31, https://doi.org/10.1016/S0013-9351(03)00142-7.